Engineering Reports

WILEY

Engineering Reports Open Access

RESEARCH ARTICLE OPEN ACCESS

Model-Based Synchronization of Dielectric Elastomers and Membrane Pumps for Performance-Optimized, Space-Efficient, and Application-Specific Pump Design

M. Baltes[1,2] | D. Bruch[2] | P. Motzki[1,2]

[1]Smart Material Systems, Center for Mechatronics and Automation Technologies (ZeMA gGmbH), Saarbrücken, Germany | [2]Intelligent Material Systems Lab, Department of Systems Engineering, Department of Materials Science and Engineering, Saarland University, Saarbrücken, Germany

Correspondence: M. Baltes (matthias.baltes@imsl.uni-saarland.de)

Received: 17 March 2025 | **Revised:** 28 May 2025 | **Accepted:** 31 May 2025

Keywords: dielectric elastomers actuators | dynamical system | electro-active polymers | resonance | vacuum pumps

ABSTRACT

This work presents a new approach to designing high-performance and efficient pumps based on dielectric elastomer actuators. By considering the entire system including load from the beginning of the design process, the advantages of dielectric elastomers are specifically utilized to minimize the required space while optimizing performance within that compact volume. The process is model-based, ensuring that every aspect, from individual components to the complete system, is carefully optimized for efficiency and power. In the case of the dielectric elastomer, the modeling approach is simplified by restricting it to cases where viscoelastic effects and time-dependent deformation are not considered. This assumption is justified by the application of clearly defined electromechanical stress limits and the exclusive focus on silicone materials, where such effects are comparatively minor. This approach represents an important step in the use of dielectric elastomer actuators for real-world applications, as the pump is more powerful over a wide working range compared to the state of the art and can therefore be used in applications where conventional pumps are still commonly employed. Although the pump already achieves mechanical performance comparable to conventional systems, it still lacks custom electronics and a smart, efficiency-optimized control system to fully leverage the advantages developed in this work. Addressing this gap forms the basis for future research.

1 | Introduction

Pumps are integral components in a wide array of everyday applications, playing a crucial role in both domestic and industrial settings. To name some prominent examples, in residential settings, pumps are used in household appliances such as washing machines, dishwashers, and heaters, ensuring a steady flow of water [1]. In the automotive industry, fuel pumps are critical for the proper operation of vehicles, supplying the necessary fuel to the engine [2]. On an industrial scale, pumps power pneumatic or vacuum grippers, and in healthcare, they are essential in a lot of medical devices [3]. Depending on the pumped medium (gas or liquid) and their applications, there are a variety of different types of pumps. Diaphragm pumps, for example, are versatile and can handle both liquids and gases, making them suitable for a wide range of applications [4, 5]. Rotary pumps are known for their efficiency in moving fluids with high viscosity, while piston pumps are designed for handling specific applications that require high pressure [6]. Additionally, peristaltic pumps are employed in applications where maintaining the purity and integrity of the fluid is crucial, such as in pharmaceutical and food industries [7]. As can be seen, pump technologies are adapted

to their specific tasks. However, most pumps are powered by conventional drives. Small pumps often use an electric engine, where the rotational motion is converted into the required type of movement. In larger systems, internal combustion engines are used [8].

This work focuses on developing an optimized pump where both the pump itself and the drive system are synchronously designed to maximize efficiency and building space according to their respective tasks and operating principles. In contrast to conventional drives, smart material transducers such as dielectric elastomers (DEs) allow for flexible design choices while inherently ensuring a compact, lightweight, and energy-efficient drive system [9–11].

In the field of DE-based pumps, various approaches have been investigated. Most commonly, two different fundamental approaches are used, employing well-known mechanisms. In addition to these, there are also new methods that implement pumping through other physical effects, presented in individual publications or prototypes [12].

The first fundamental approach integrates the DE both as the driving mechanism and as a structural component of the pump mechanism itself. This dual role often restricts the pump's capability to handle specific pressure loads (due to the DE's stretch ability) or to pump certain types of media (due to compatibility issues between the DE material and the pumped medium) [13–18]. This approach can yield interesting foundational concepts but significantly limits the range of potential applications. In contrast, the second approach involves using a pump mechanism that has already been designed for the application using conventional drives [19]. In this case, a DE drive is developed to meet the requirements of the conventional drive and replace it. In this approach, the scope of application is not limited. However, the pump mechanism is not optimized for a DE-based drive, which could lead to inefficient or uneconomical outcomes.

To address the challenge of designing an optimized pump based on DEs for everyday applications, this paper adopts a new approach. Similar to the second approach mentioned earlier, a conventional membrane pump mechanism is utilized. However, instead of employing a fixed design, this mechanism is fully parameterized and modeled. Concurrently, the DE drive is also modeled and simulated, allowing for iterative optimization of both components [20, 21]. In this work, the focus is limited to silicone-based DEs. Compared to acrylic-based elastomers, silicone exhibits only minor viscoelastic and time-dependent effects. As a result, these effects are not considered in the presented model. Furthermore, the maximum mechanical deformation is restricted to 50%, which ensures that no plastic deformation occurs. The applied electric field is also conservatively chosen to be 15% below the level used in production tests and 5% below the manufacturer's specified breakdown strength. These measures help to avoid critical failure scenarios caused by inhomogeneities or moisture-related influences that could reduce the dielectric strength, and, therefore, such cases are not further considered in the model. However, the overall concept presented in this work can also be extended by combining it with more advanced DE models that account for such effects. This allows for a broader selection of materials and parameters, which can be beneficial in optimization processes [22–24]. The parallel optimization process of the pump mechanism and drive system aims to enhance the effectiveness of the overall system. The model-based design methodology of an entire pump system based on a DE drive is described in this paper and is validated by designing and constructing a pump with specific requirements. In conventional applications, two key parameters are often specified that are critical for determining functionality: the maximum differential pressure (or target absolute pressure) and the free flow.

In addition to these two performance-specific requirements, the size of the installation space plays a decisive role. Consequently, these three requirements form the basis for our design. Step by step, the individual components can then be designed. It is important to consider the interdependence of the individual components and how they influence each other's design.

The structure of the paper is designed to provide a schematic approach to the design of an optimized pump, considering the resulting dependencies. In the Supporting Section, the material selection, design, and fabrication of the individual components required for a DE-based pump are detailed. Different design variations are presented, and a meaningful selection for the

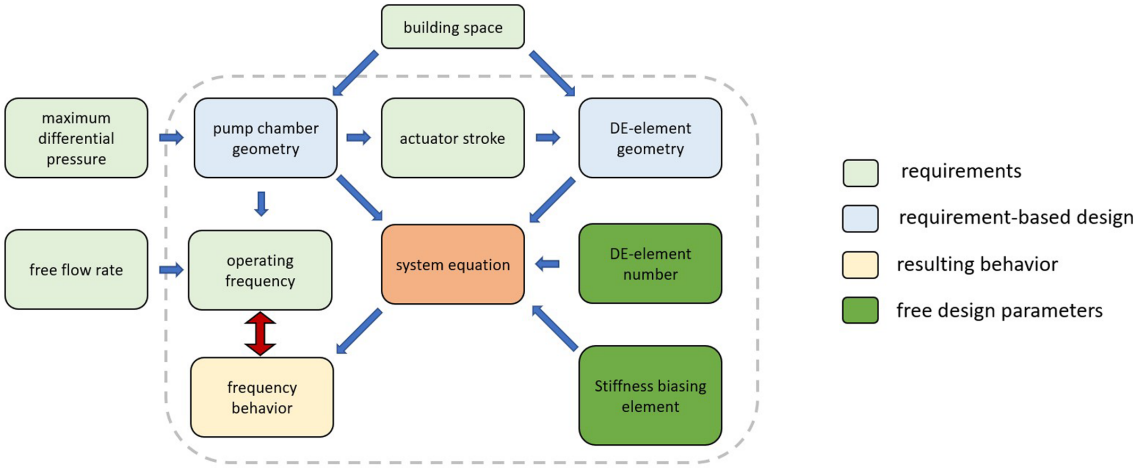

FIGURE 1 | Systematic relationships and procedures throughout the pump design process.

pump casing is made. The main paper begins with the overall pump model design, followed by the validation of both the model and the pump's performance to ensure they meet the specified requirements. The paper concludes with a final evaluation and discussion. The model and later the design of the optimized pump follow the structure outlined in Figure 1. The free design parameters for iterative optimization are the number of DE elements and the biasing mechanism. Since the number of DE elements scales the total force linearly and the biasing mechanism can be chosen with a linear force–displacement characteristic, these two variables can be easily utilized as design parameters and incorporated into the model without prior validation. In the subsequent chapter, the model is used to design an optimized pump. For this purpose, the equation of motion is solved, and unknown parameters such as the moving mass and damping are determined through initial experiments, iteratively improving the equation of motion. In the final step, a prototype of the pump is designed, and the final requirements are validated based on this prototype.

2 | Modeling and Simulation of the Pump System

2.1 | Model-Based Equation of Motion

In this section, the system equation for the pump will be established based on the DE, the biasing element, the pump chamber, and the applied load pressure. These individual components are specially designed, manufactured, and validated for the purpose of determining the model. The exact selection and details of this process are provided in the attached Supporting Information.

To formulate the equation of motion, the three forces F_{De}, F_{bias}, F_{chamber}, as well as the system damping d_{damp}, must be determined either experimentally or through modeling. Figure 2 shows the forces and their directions of action with respect to the generally chosen coordinate system.

$$m\ddot{x} = -d_{damp}\dot{x} - F_{DE} + F_{bias} + F_{chamber} \tag{1}$$

As described in Section S2, the biasing element will be limited to springs with constant stiffness (either positive or negative). The force of the biasing element F_{bias} can thus be easily calculated based on its stiffness C_{bias} and preload $x_{0\,\mathrm{bias}}$. These two parameters are kept general and as design parameter for the system.

$$F_{\mathrm{bias}} = c_{bias}\left(\mathrm{x} - \mathrm{x}_{0\,\mathrm{bias}}\right) \tag{2}$$

The second force–displacement characteristic needed is that of the pump chamber itself. Several factors play a role here, including the geometry of the chamber and pump membrane, the pressure-dependent force on the pump membrane, and finally, the switching points of the check valves. The maximum stroke is determined by the bistability of the pump membrane and its two stable states. Beyond this point, the pump membrane acts as a hard stop for the system. The first component of the force is the stiffness of the pump membrane itself, while the second component is due to the pressure acting on the pump membrane. The stiffness of the pump membrane was experimentally determined in the previous chapter and can be neglected due to its small force relative to the pressure-dependent component.

The force generated by the pressure f_{pressure} can be calculated based on the pressure difference Δp between the inside of the pump chamber p_{chamber} and the ambient p_{ambient}, multiplied by the area of the pump membrane A_{membrane} in the direction of the force.

$$\Delta p = p_{chamber} - p_{ambient} \tag{3}$$

$$F_{pressure} = \Delta p \mathrm{A}_{\mathrm{membrane}} \tag{4}$$

To calculate the force, it is necessary to know the pressure inside the pump chamber. This pressure depends on the pressure applied at the inlet/outlet valves, the position-dependent compression of the volume within the pump chamber, and the status of the valves. Different phases of a pump cycle must be distinguished (Figure 3), which vary depending on the direction of membrane movement and the pressures at the two valves. When the pump membrane reduces the volume inside the chamber, it is referred to as the compression phase, where the pressure increases. If the pressure inside the chamber is as high as that at the outlet valve, plus the additional pressure required to open the valve, the outlet valve opens, and the fluid can expel through it. This phase is referred to as the discharge phase and continues until the direction of movement of the pump membrane changes again. During the discharge phase, the pressure inside the chamber remains constant, and so does the force component resulting from the pressure. As the membrane moves back to its initial position, the volume inside the pump chamber increases again, and the pressure decreases. In the so-called relaxation phase, accordingly, the pressure-dependent force also decreases. The phase ends when the pressure within the chamber equals the pressure applied at the inlet valve, considering the responding pressure of that valve. In the fourth and final phase, known as the suction phase, the valve draws new fluid into the chamber. The inlet valve remains open, and the pressure remains constant.

For known constant pressures at the inlet and outlet valves, determining the pressure-dependent force is straightforward. In a practical application, the goal of the pump is to generate either an overpressure or a vacuum. In the case of overpressure, this means that the pressure at the inlet valve remains constant while

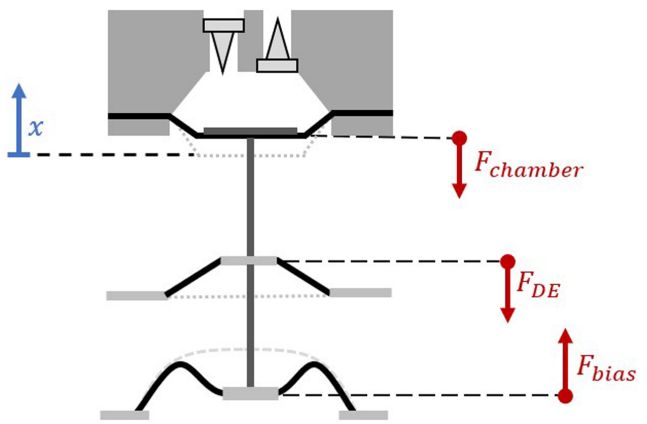

FIGURE 2 | Free-body diagram of the force equilibrium for the complete system.

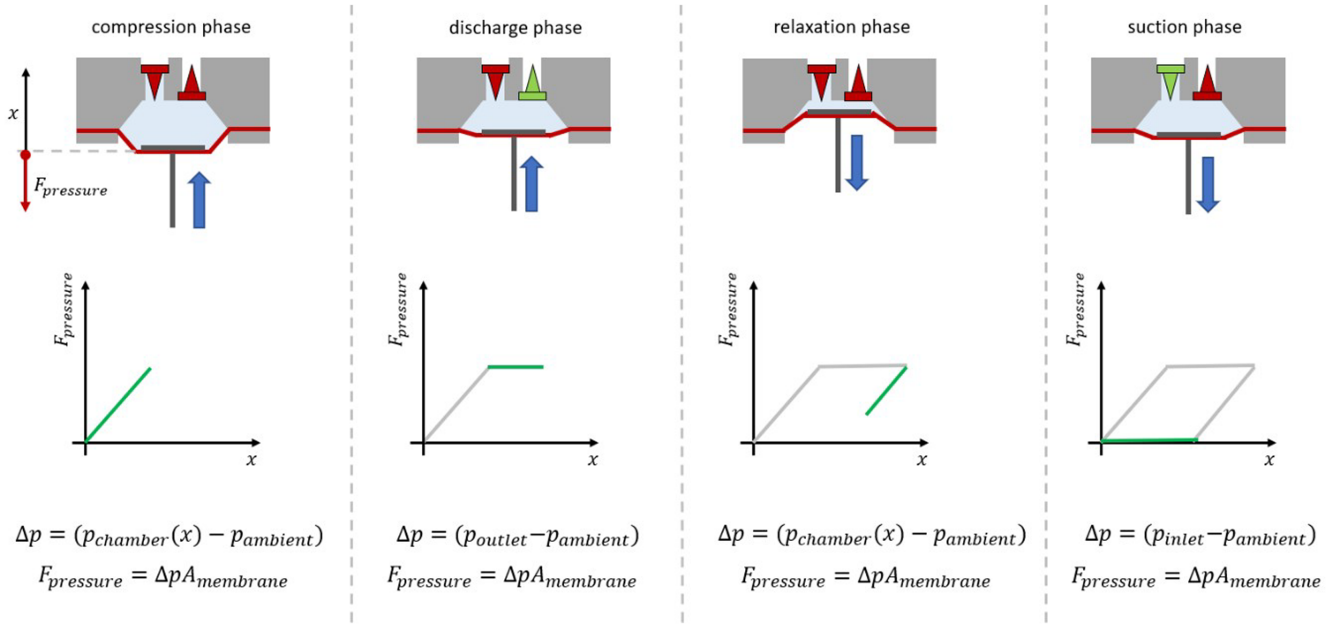

FIGURE 3 | The four phases of a diaphragm pump cycle.

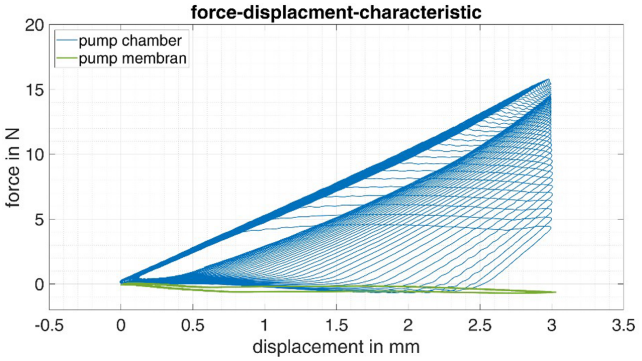

FIGURE 4 | Load force model, for example, pressures compared to the validation measurements.

it varies at the outlet valve. Conversely, for a vacuum pump, the situation is reversed. Thus, the point at which the valve with variable pressure opens also changes accordingly.

Based on these two measurements, which were conducted during the component manufacturing process (Figure S8), the pressure-dependent model of the load force can be validated. By neglecting the inherent force of the pump membrane, the load force generated by the volume compression is considered here. As an example, Figure 4 shows the load forces resulting from the model for three different load pressures.

In this comparison, the linear relationship between stroke (pump volume compression) and load pressure (Equation 4) can be confirmed through the resulting maximum forces generated by the different load pressures. Additionally, the valve switching times align well between the model and the measurement, further validating the linear relationship.

The four different phases must also be separately considered in the system equation, along with the conditions under which each phase changes. The transition between the suction and compression phases, as well as between the discharge and relaxation phases, corresponds to the reversal points in the motion of the pump membrane where the membrane velocity is zero $x(t) =. 0$ These conditions can thus be considered when solving the system equation. Complications arise due to the switching points of the valve with variable pressure. Because the construction space of the pump chamber is nearly cylindrical, a linear relationship is assumed between the movement of the pump membrane and the compression of the pump volume. Also, the pressure within the chamber then linearly depends on the membrane's stroke. Given a specified load pressure and the known activation pressure of the valves, the point at which the valve opens can be calculated based on the stroke of the membrane and the behavior of the membrane from the previous cycle. The behavior from the previous cycle is crucial because it accounts for scenarios where the membrane does not fully return to its initial position. In such cases, the starting volume for the subsequent cycle is less than the maximum volume.

The information from the previous cycle is indicated in the system equation by the x_i in $\Delta(x, x_i)$. In the schematic representation shown in Figure 5, the system equation is solved considering the different phases. Each phase of the pump cycle is solved sequentially, with the end conditions of one phase serving as the initial conditions for the subsequent phase. This sstep-by-step approach ensures accurate modeling of the pump's dynamic behavior. The goal is to analyze the frequency response of the pump under various load pressures using the system equation. The load pressure corresponds to the application-specific pressure at the inlet valve in the case of a vacuum pump or the pressure at the outlet valve in the case of an overpressure pump.

The last component to be modeled is the DE element. Using the experiment from Figure S9, the characteristic curve for 0 and 2300 V is known. Based on the force–displacement data obtained at these two fixed voltage levels, a numerical model for

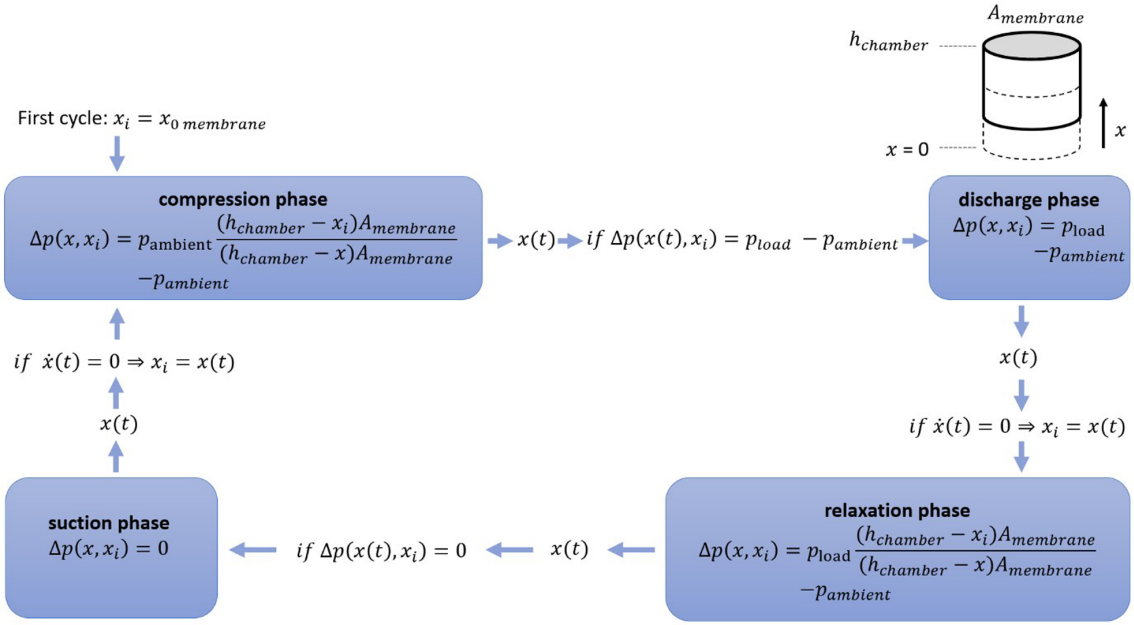

FIGURE 5 | Schematic approach to solving the equation of motion.

arbitrary voltages can be derived. The two characteristic curves are interpolated using a second-degree polynomial, which is appropriate due to the geometry of the COPs. Since the force is known to depend quadratically on the applied voltage, a mathematical model, such as the one proposed in Equation (5), can be employed to capture this relationship. The parameters a, b, and c are then determined from the interpolated characteristic curves for (0 V, x) and (2300 V, x).

$$F_{DE}(U, x) = U^2(ax^2 + bx + c) \tag{5}$$

With Equation (8), the force–displacement characteristic for a single DE element can be described.

To adapt the force of the actuator to the pump application and perfectly match it, the number of DE elements (n_DE) is used as a design parameter. This ensures that the actuator performs enough work under operating conditions to guarantee the pump's performance, while simultaneously keeping the number of elements minimal to operate as efficiently as possible (energy-saving, no over-dimensioned actuator) and with minimal costs.

$$m\ddot{x} = -d_{damp}\dot{x} - n_{DE}F_{DE}(U(t), (x - x_{0\ DE})) + c_{bias}(x - x_{0\ bias}) + F_{membrane}(x) + \Delta p(x, x_i)A_{membrane} \tag{6}$$

Since all individual components of the pump have been described and modeled, the equation of motion (1) can now be described in more detail. In this equation, the number of DE elements c_{bias} and the stiffness of the biasing mechanism F_{DE} are variable design and optimization parameters. The DE force F_{DE} is described through the numerical model (5), the pump membrane force F_{membrane} is negligible and can be assumed to be 0, and the load force dependency ($\Delta p(x, x_i)A_{\text{membrane}}$) is described using the approach and the model from Figure 5. The only unknowns needed to solve the equation are the freely moving mass and the damping of the system d_{damp}. These are determined in the next chapter through experimental procedures. For this purpose, they are initially assumed and then iteratively determined through the experiments.

2.2 | Solving of the System Equation

Building on the previous measurements and modeling of the individual components, all external forces in the system equation are now known. To solve the equation, the two remaining parameters, the freely movable mass and the system damping, must be determined experimentally. For this purpose, a small test rig (Figure 6) is constructed using the previously fabricated components. The individual components are mounted with adjustable spacing on an aluminum profile and connected via a central axis. This adjustable setup allows the operating points of the individual components to be precisely configured. Preliminary experiments revealed that four DE-elements are required to achieve a displacement range suitable for validation purposes. A combination of an NBS (negative rate bias spring) and an LBS (positive rate bias spring) is used as the pre-tension mechanism. This configuration offers the advantage of enabling a wide range of stiffness values to be tested, from negative to positive. Additionally, the positive stiffness spring ensures that the operating point can always be adjusted precisely, independent of the stiffness being tested.

Using this experimental setup, two measurements can be performed to determine the freely movable mass and the damping of the system. These measurements require two frequency responses of the system, each with a different system stiffness. For this purpose, two linear springs with known stiffness values are integrated into the test rig. To obtain the frequency response, the DE elements are driven with a sinusoidal voltage of increasing frequency and constant amplitude (2300 V). The displacement of the system is measured using a laser sensor. To determine the freely movable mass, the resonance frequency

is identified from the frequency response. In an underdamped system, this resonance frequency depends solely on the freely movable mass and the system stiffness.

$$f_r = \sqrt{\frac{c_{\text{system}}}{m_{\text{free}}}} \tag{7}$$

By conducting two measurements with different spring stiffnesses and utilizing the known stiffness of the two linear springs, a system of equations can be established. This system allows the elimination of the unknown residual system stiffness, enabling the calculation of the freely movable mass.

$$f_{r\,LBS1} = \sqrt{\frac{c_{\text{system without biasining}} + c_{\text{bias }LBS1}}{m_{\text{free}}}}$$

$$f_{r\,LBS2} = \sqrt{\frac{c_{\text{system without biasining}} + c_{\text{bias }LBS2}}{m_{\text{free}}}} \tag{8}$$

The final missing parameter required to solve the differential equation is the damping of the system. To determine this, one of the previously conducted experiments can be used. The parameters from this experiment are substituted into the system equation, which is then solved using the same input voltage signal as the experiment. As an initial estimate for the damping constant, a starting value of 0.5 kg/s is assumed. When comparing the frequency responses from the measurement and the simulation, it is observed that the resonance frequencies align. However, the amplitude at resonance is influenced by the damping: if the damping value is too high, the simulated amplitude will be smaller than the measured one; if the damping value is too low, the simulated amplitude will be larger. By iteratively adjusting the damping value and re-simulating, the damping constant can be fine-tuned until the simulated and measured frequency responses match. This ensures accurate determination of the system damping for solving the differential equation. The validation is performed by running the model for the second experiment and comparing the resulting frequency responses. This process is demonstrated later in this work, where the simulation and measurement using the optimized parameters are employed for the final pump design.

With the damping constant and the freely movable mass now determined, the system is fully characterized, allowing for the design of a pump optimized to meet the specified goals. The design parameters in this case include the stiffness of the pretension mechanism, the number of DE-elements, and the operating point, which corresponds to the pre-tension of individual components. The objective is to find a configuration in which the pump reaches a load pressure of 1000 mbar (ambient pressure) while achieving a minimum displacement of 3 mm. It should also achieve the same 3 mm displacement at a load pressure of 300 mbar.

Through iterative testing, it is determined that an operating frequency of 50 Hz is sufficient to achieve the desired flow for the pump chamber design at 0 mbar load pressure. Both the volume and the properties of the valves play a role in this. This was not thoroughly considered earlier, as the operating frequency is flexible, and for optimal operation, the resonance can always be adjusted to the desired frequency by modifying the system stiffness. If the requirement is for the pump to operate at a specific frequency, this can be precisely planned through measurements with the pump chamber and its design, after which other parameters, as shown here, can be adjusted accordingly. The operating point is adjusted to ensure that each DE element is in static equilibrium at a displacement of 7.5 mm, thereby ensuring that the electric field remains small enough at maximum displacement to prevent damage to the DE element. The number of DE elements is used to control the amplitude. If the amplitude is less than the required 3 mm, the actuator cannot produce sufficient work to

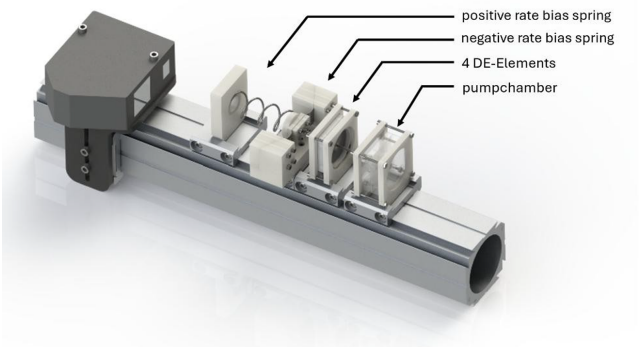

FIGURE 6 | Experimental setup for determining the missing system parameters.

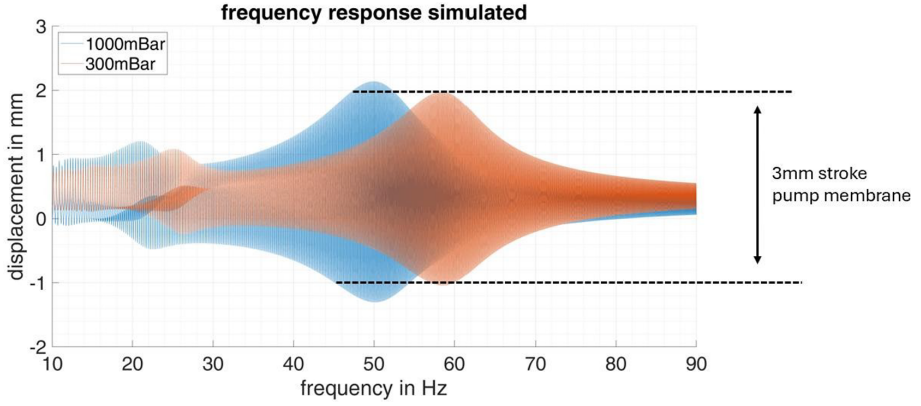

FIGURE 7 | Frequency response simulated pump design.

generate the required pumping power. If the amplitude is much larger, the actuator is oversized. The number of DE elements also affects system stiffness; therefore, after adjusting this design parameter, the stiffness of the pretensioning element must also be modified to achieve the desired operating frequency. Figure 7 illustrates the simulated frequency response. The results reveal a load-dependent shift in the resonance frequency. At ambient pressure, the resonance frequency aligns with the planned 50 Hz, while at minimal target pressure, it increases to approximately 60 Hz. This shift can be attributed to a change in stiffness, which arises from the additional force exerted on the pump membrane due to the load pressure. The analysis also shows that the target stroke of 3 mm is accurately achieved at maximum pressure, whereas at 0 mbar, the stroke slightly exceeds this value. This behavior is explained by the reduction in maximum amplitude with increasing frequency, given the same configuration and input energy. To ensure consistent pressure generation independent of load, the pump must be slightly oversized for operation at ambient pressure. However, in the final configuration, the pump membrane acts as a hard stop in both directions, limiting the maximum stroke to 3 mm.

To validate the model, the next step involves building and testing the final prototype. For this purpose, the missing component, the preload mechanism required to achieve the stiffness chosen in the simulated pump of Figure 7, is designed and integrated with the components that have already been manufactured.

3 | Prototype Fabrication and Model Validation

The DE elements and the pump chamber have already been manufactured and characterized for the validation of the individual models. The final component required for the prototype is the preload mechanism. Since a negative stiffness is needed, a Negative Rate-Based Spring (NBS) is chosen. This consists of two compressed beams arranged in a crossed configuration. The geometry of the beams is adjusted so that, when clamped, they have the same footprint as the DE elements and the pump chamber. The desired geometry for the NBS characteristics is determined through simulation [25]. Once defined, the beams are laser-cut from spring steel and integrated into a clamp made from Formlabs Rigid (chosen for its resistance to deformation under high forces). Next, the finished NBS are characterized to ensure that their behavior matches the characteristics predicted in the simulation.

The individual components of the pump can then be assembled. It is crucial that the parts are connected using spacers to ensure that each component is positioned at its desired operating point. The components are secured on the central axis with M2 nuts, as done in previous experiments. The next component is then attached, followed by another M2 nut. The outer frames are placed with spacers, accounting for the preload plus the thickness of the M2 nuts, ensuring proper alignment. To maintain the mass unchanged, neither the length of the axis nor the number of nuts used is altered. The completed assembly is shown in Figure 8. Since the footprint is set to 45 mm × 45 mm, and the individual components result in a height of 80 mm, the overall dimensions of the pump would be 45 mm × 80 mm.

The design method is then validated using this pump prototype. To do this, the frequency response, as well as the two desired specifications (flow and pressure) are measured. In the first step, the system's resonance frequency is determined by measuring the frequency response. As described in the previous chapter, the pump is driven with a sinusoidal voltage with increasing frequencies, and the displacement of the moving axis is measured using a laser displacement sensor (Keyence LK-G87). In the completed pump setup, this measurement is taken at the underside of the NBS.

In the first measurement, this is done without load pressure at the inlet valve. A second measurement is then performed with an absolute pressure of 300 mbar at the outlet valve. The frequency response for the two different pressures is shown in Figure 9. The resonance frequencies correspond to those determined in the simulation and the desired frequencies specified in the requirements. However, the response curve appears asymmetric compared to the simulation. This asymmetry can be explained by the pump chamber itself, as the pump membrane acts as a hard stop in one direction, and the chamber acts as a hard stop in the other direction. These hard stops were not considered in the model, as the pump is designed to ideally oscillate from one hard stop to the other, minimizing energy loss. Since the amplitude decreases with increasing pressure, this can only be implemented for the maximum load pressure.

What is crucial for the pump's functionality is that it generates a stroke of around 3 mm at maximum pressure. This is ensured for a driving frequency of 62 Hz, which is the resonance frequency at maximum pressure. The pump is driven with a sinusoidal voltage at 62 Hz and allowed to operate against a closed volume,

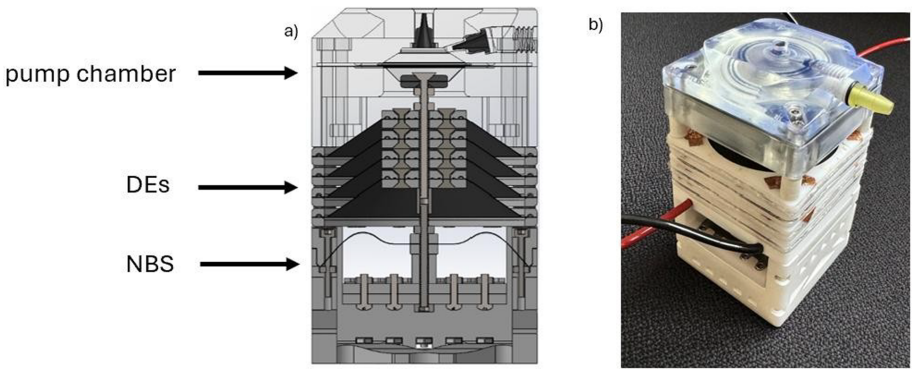

FIGURE 8 | Cross-section of the final pump design (a) and the completed assembled prototype (b).

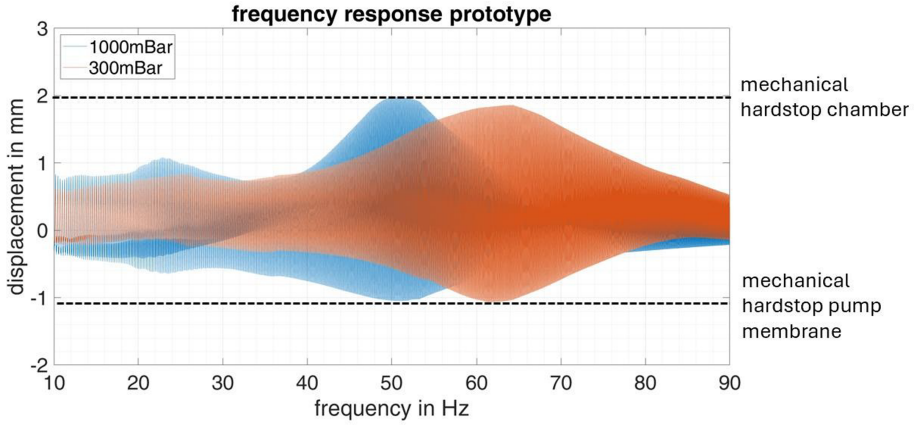

FIGURE 9 | Experimentally acquired frequency response of the final pump prototype.

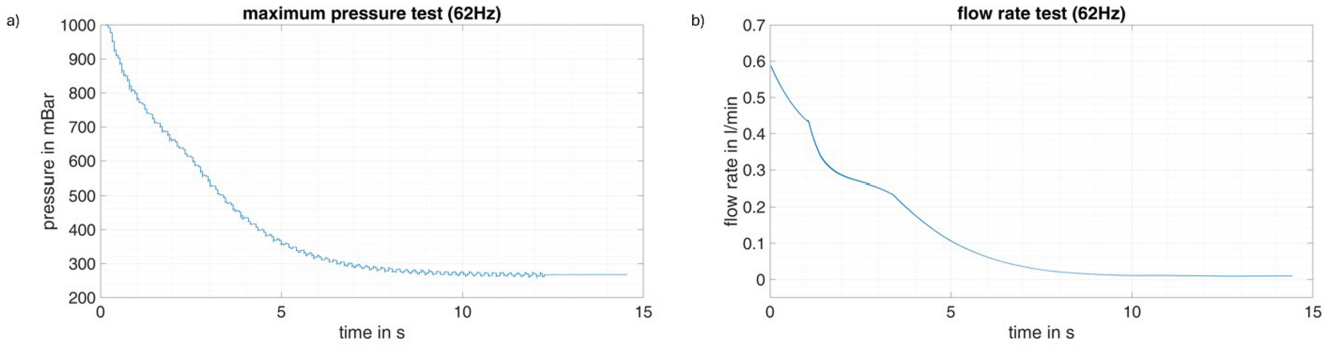

FIGURE 10 | Pump specification validation: (a) max pressure and (b) flow rate.

while both flow and pressure are recorded simultaneously. For the chosen pressure tank, the minimum absolute pressure is reached after about 12 s, measuring 267 mbar (Figure 10), which is approximately the maximum performance measured previously at the pump chamber itself using a linear actuator. The selected actuator is, therefore, sufficiently strong to displace the pump by 3 mm at maximum pressure, ensuring proper function.

The maximum free flow is read at the start of the measurement and is 0.6 L/min (Figure 10), which is slightly higher than the requirement. Since the measurement is performed at 62 Hz, the maximum amplitude at 0 mbar load pressure is less than 3 mm. As a result, with a driving frequency of 50 Hz, a larger free flow would be achieved, but the desired target pressure would no longer be reached because the pump would not achieve the target stroke of 3 mm at maximum pressure. The desired requirements have been met, and the functionality of the design method has been successfully validated.

4 | Conclusion and Discussion

This work has demonstrated that, unlike conventional approaches, a DE-based pump can be optimally designed for a specific application by considering all components of the system. Each component has been analyzed and parameterized to derive the pump's equation of motion. Through a case study, the design process for an optimal pump has been shown step by step, and the approach has been validated with a prototype, confirming that the pump meets the required specifications. The pump has been found to operate optimally at the desired resonance frequency for maximum pressure. It has been observed that resonance frequency shifts depending on the load pressure. To ensure optimal operation, the pump should ideally always run in resonance. Additionally, it has been shown that the maximum voltage amplitude is only required at maximum load pressure, allowing the amplitude to be reduced at lower pressures and, consequently, at lower operating frequencies. Future work will involve implementing a smart control system using an external load pressure sensor. Once validated, the self-sensing effect of the DEs will be utilized to control the pump and replace the external sensor. Since the pump operates from hard stop to hard stop, unlike traditional DE self-sensing methods, capacitance cannot be used as a control variable. Instead, energy analysis of the system will allow for load pressure estimation. It has been determined that the pump performs different amounts of work depending on the pressure, with minimal work occurring at maximum load pressure. By analyzing the total energy required to charge and discharge the DEs, energy losses during the pump cycle can be quantified, enabling optimization of the system's energy efficiency. Additionally, a series connection of multiple pumps, operating anti-cyclically and reusing the energy of the DEs, could be explored to further improve efficiency in the future.

The pump is thus the first DE-based pump that matches the output power of an industrial pump without compromising on space. Compared to state-of-the-art DE-based pumps, it is significantly

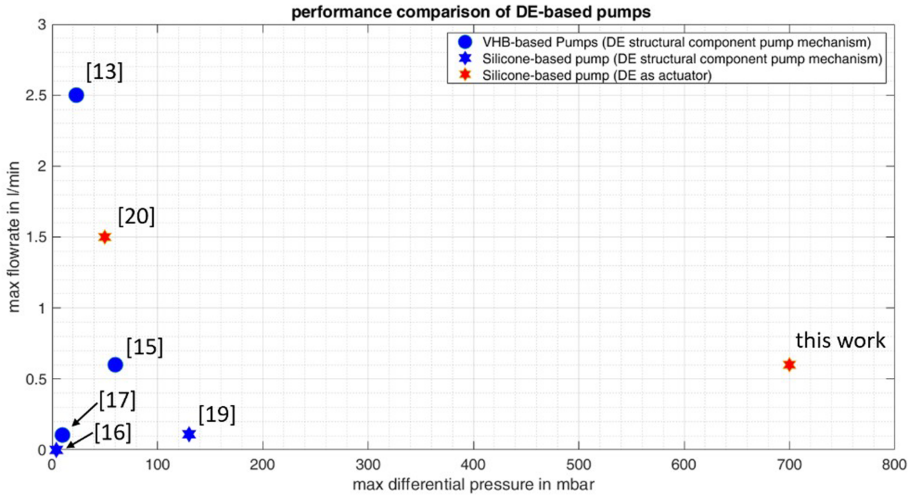

FIGURE 11 | Overview: Performance state of the art DE-based pumps.

more powerful and can be optimized for specific applications to deliver optimal performance tailored to the desired specifications. Figure 11 provides an overview of comparable DE-based pumps.

The pumps were designed for various specific applications, making direct comparisons challenging. It is evident that only two pumps ([13, 19]) in a given range offer higher performance, but only for very low pressures, up to 50 mBar. This severely limits their practical use. As fluid pumps in household appliances, heat pumps, and similar systems must be able to pump water over significant distances and heights, a 50 mBar pressure would only allow for a lift of about 50 cm, which makes such pumps unsuitable for these types of applications. Compressors, on the other hand, are often required to generate air pressures of several bars. While low-pressure applications are easier to implement due to the smaller forces involved, they are rarely found in practical real-world applications. With the design methodology presented in this paper, a pump has been developed for the first time that can replace those currently operated with conventional actuators and can be utilized in real-world applications. With the next steps outlined here, this pump can now be further developed into a self-regulating smart pump, making it not only comparable to existing technologies but also smarter and superior.

Author Contributions

M. Baltes: writing – original draft, validation, data curation, project administration, investigation, visualization, formal analysis. **D. Bruch:** writing – review and editing. **P. Motzki:** supervision, writing – review and editing.

Acknowledgments

Open Access funding enabled and organized by Projekt DEAL.

Conflicts of Interest

The authors declare no conflicts of interest.

Data Availability Statement

The data that support the findings of this study are available from the corresponding author upon reasonable request.

References

1. M. Z. Youssef, "Design and Performance of a Cost-Effective BLDC Drive for Water Pump Application," *IEEE Transactions on Industrial Electronics* 62, no. 5 (2015): 3277–3284, https://doi.org/10.1109/TIE.2014.2350461.

2. U. Kemmner, M. Rollwage, and K. Rose, *New Generation of BOSCH Electrical Fuel-Pumps—Improvement in Hot-Fuel Handling and Noise* (FID, 1987), https://doi.org/10.4271/870120.

3. L. Cao, S. Mantell, and D. Polla, "Design and Simulation of an Implantable Medical Drug Delivery System Using Microelectromechanical Systems Technology," *Sensors and Actuators, A: Physical* 94, no. 1 (2001): 117–125, https://doi.org/10.1016/S0924-4247(01)00680-X.

4. K. Zhao, Y. Lou, G. Peng, C. Liu, and H. Chang, "A Review of the Development and Research Status of Symmetrical Diaphragm Pumps," *Symmetry* 15 (2023): 2091, https://doi.org/10.3390/sym15112091.

5. K. M. Pos, "Drug Transport Mechanism of the AcrB Efflux Pump," *Biochimica et Biophysica Acta, Proteins and Proteomics* 1794, no. 5 (2009): 782–793, https://doi.org/10.1016/j.bbapap.2008.12.015.

6. S. Yedidiah, *Centrifugal Pump User's Guidebook* (Springer Science & Business Media, 1996).

7. J. Klespitz and L. Kovács, "Peristaltic Pumps—A Review on Working and Control Possibilities," in *2014 IEEE 12th International Symposium on Applied Machine Intelligence and Informatics (SAMI)* (2014), 191–194, https://doi.org/10.1109/SAMI.2014.6822404.

8. H. A. Humphrey, "An Internal-Combustion Pump, and Other Applications of a New Principle," *Proceedings of the Institution of Mechanical Engineers* 77, no. 1 (1909): 1075–1200, https://doi.org/10.1243/PIME_PROC_1909_077_019_02.

9. E. Hajiesmaili and D. R. Clarke, "Dielectric Elastomer Actuators," *Journal of Applied Physics* 129, no. 15 (2021): 151102, https://doi.org/10.1063/5.0043959.

10. Z. Xing, J. Zhang, D. McCoul, Y. Cui, L. Sun, and J. Zhao, "A Super-Lightweight and Soft Manipulator Driven by Dielectric Elastomers," *Soft Robotics* 7, no. 4 (2020): 512–520, https://doi.org/10.1089/soro.2018.0134.

11. J. Zhang, J. Chen, and Z. Ren, "Mechanical Behavior of a Circular Dielectric Elastomer Membrane Under Out-Of-Plane Deformation," *Journal of Mechanics* 37 (2020): 184–191, https://doi.org/10.1093/jom/ufaa026.

12. M. Smith, V. Cacucciolo, and H. Shea, "Fiber Pumps for Wearable Fluidic Systems," *Science* 379, no. 6639 (1979): 1327–1332, https://doi.org/10.1126/science.ade8654.

13. G. Mao, L. Wu, Y. Fu, et al., "Design and Characterization of a Soft Dielectric Elastomer Peristaltic Pump Driven by Electromechanical Load," *IEEE/ASME Transactions on Mechatronics* 23, no. 5 (2018): 2132–2143, https://doi.org/10.1109/TMECH.2018.2864252.

14. N. Goulbourne, M. I. Frecker, E. M. Mockensturm, and A. J. Snyder, "Modeling of a Dielectric Elastomer Diaphragm for a Prosthetic Blood Pump," in *Smart Structures and Materials 2003: Electroactive Polymer Actuators and Devices (EAPAD)*, ed. Y. Bar-Cohen (SPIE, 2003), 319–331, https://doi.org/10.1117/12.484388.

15. S. Ho, H. Banerjee, Y. Y. Foo, et al., "Experimental Characterization of a Dielectric Elastomer Fluid Pump and Optimizing Performance via Composite Materials," *Journal of Intelligent Material Systems and Structures* 28, no. 20 (2017): 3054–3065, https://doi.org/10.1177/1045389X17704921.

16. P. Lotz, M. Matysek, and H. F. Schlaak, "Fabrication and Application of Miniaturized Dielectric Elastomer Stack Actuators," *IEEE/ASME Transactions on Mechatronics* 16, no. 1 (2011): 58–66, https://doi.org/10.1109/TMECH.2010.2090164.

17. Y. Wang, Z. Li, L. Qin, G. Caddy, C. H. Yap, and J. Zhu, "Dielectric Elastomer Fluid Pump of High Pressure and Large Volume via Synergistic Snap-Through," *Journal of Applied Mechanics* 85, no. 10 (2018): 101003, https://doi.org/10.1115/1.4040478.

18. J. Chavanne, J. Haenni, T. Martinez, et al., "Manufacturing and Tests of a Tubular Multilayer Dielectric Elastomer Actuator for an Impedance Pump," in *2020 23rd International Conference on Electrical Machines and Systems (ICEMS)* (IEEE, 2020), 380–383, https://doi.org/10.23919/ICEMS50442.2020.9290904.

19. P. Linnebach, G. Rizzello, and S. Seelecke, "Design and Validation of a Dielectric Elastomer Membrane Actuator Driven Pneumatic Pump," *Smart Materials and Structures* 29 (2020): 075021, https://doi.org/10.1088/1361-665X/ab8a01.

20. D. Meng, Y. Li, C. He, J. Guo, Z. Lv, and P. Wu, "Multidisciplinary Design for Structural Integrity Using a Collaborative Optimization Method Based on Adaptive Surrogate Modelling," *Materials and Design* 206 (2021): 109789, https://doi.org/10.1016/j.matdes.2021.109789.

21. D. Meng and S.-P. Zhu, *Multidisciplinary Design Optimization of Complex Structures Under Uncertainty* (CRC Press, 2024), https://doi.org/10.1201/9781003464792.

22. C. Farmer and H. Medina, "Effects of Electrostriction on the Bifurcated Electro-Mechanical Performance of Conical Dielectric Elastomer Actuators and Sensors," *Robotica* 41, no. 1 (2023): 215–235, https://doi.org/10.1017/S0263574722001254.

23. H. Medina, C. Farmer, and I. Liu, "Dielectric Elastomer-Based Actuators: A Modeling and Control Review for Non-Experts," *Actuators* 13, no. 4 (2024): 151, https://doi.org/10.3390/act13040151.

24. D. Korn, C. Farmer, and H. Medina, "A Detailed Solution Framework for the Out-Of-Plane Displacement of Circular Dielectric Elastomer Actuators," *Engineering Reports* 4, no. 1 (2022), https://doi.org/10.1002/eng2.12442.

25. M. Hodgins and S. Seelecke, "Mechanical Behavior of a Bi-Stable Negative-Rate Bias Spring System," in *Proceedings of SPIE—The International Society for Optical Engineering* (SPIE, 2010), 7644, https://doi.org/10.1117/12.852373.

Supporting Information

Additional supporting information can be found online in the Supporting Information section. **Data S1.** Supporting Information.